Contents lists available at ScienceDirect

Computers in Biology and Medicine

Analyzing the effect of electrode size on electrogram and activation map properties

Bahareh Abdi [a],[*], Mathijs S. van Schie [b], Natasja M.S. de Groot [b], Richard C. Hendriks [a]

[a] *Circuits and Systems (CAS) Group, Delft University of Technology, the Netherlands*
[b] *Department of Cardiology, Erasmus University Medical Center, the Netherlands*

ARTICLE INFO

ABSTRACT

Background: Atrial electrograms recorded from the epicardium provide an important tool for studying the initiation, perpetuation, and treatment of AF. However, the properties of these electrograms depend largely on the properties of the electrode arrays that are used for recording these signals.

Method: In this study, we use the electrode's transfer function to model and analyze the effect of electrode size on the properties of measured electrograms. To do so, we use both simulated as well as clinical data. To simulate electrogram arrays we use a two-dimensional (2D) electrogram model as well as an action propagation model. For clinical data, however, we first estimate the *trans*-membrane current for a higher resolution 2D modeled cell grid and later use these values to interpolate and model electrograms with different electrode sizes.

Results: We simulate electrogram arrays for 2D tissues with 3 different levels of heterogeneity in the conduction and stimulation pattern to model the inhomogeneous wave propagation observed during atrial fibrillation. Four measures are used to characterize the properties of the simulated electrogram arrays of different electrode sizes. The results show that increasing the electrode size increases the error in LAT estimation and decreases the length of conduction block lines. Moreover, visual inspection also shows that the activation maps generated by larger electrodes are more homogeneous with a lower number of observed wavelets. The increase in electrode size also increases the low voltage areas in the tissue while decreasing the slopes and the number of detected deflections. The effect is more pronounced for a tissue with a higher level of heterogeneity in the conduction pattern. Similar conclusions hold for the measurements performed on clinical data.

Conclusion: The electrode size affects the properties of recorded electrogram arrays which can respectively complicate our understanding of atrial fibrillation. This needs to be considered while performing any analysis on the electrograms or comparing the results of different electrogram arrays.

1. Introduction

Recording and processing of electrograms (EGMs) is the cornerstone of mapping procedures guiding ablative therapies of cardiac arrhythmias. Thorough understanding of the impact of recording technology on EGM morphology is of paramount importance, particularly in case of complex tachyarrhythmias such as atrial fibrillation (AF) [1,2]. However, the properties of these electrograms depend to a large extent on the physical dimensions of the electrode arrays that are used for recording these signals.

As shown in several studies, the electrode's size (or diameter) is an important parameter that can affect the characteristics of the recorded electrograms. Most studies focus on bipolar electrograms and measurements that are performed only on clinical recordings [3–7]. There are only a few studies investigating the effect of the electrode size on the properties of the unipolar electrograms using both electrophysiological models and clinical recordings. These properties include signal-to-noise ratio (SNR), fractionation level, voltage level, and the error in local activation time (LAT) estimation [8–10]. In general, these studies show that increasing the electrode size increases the SNR and consequently the atrial activity is less affected by noise and artifacts [11,12]. However, this is mainly the case for homogeneous tissue. It has also been shown that the number of deflections and the level of fractionation also increases by increasing the electrode size [7–9]. Moreover, low voltage areas in the tissue also increase when using bigger electrode sizes [6,8]. It has also been shown that using larger electrodes, increases

the error in LAT estimation [10], which will result in activation maps with less detail and less conduction blocks [3,5]. These effects are more pronounced in zones of conduction block or slow conduction in the tissue (i.e., scarred tissue) [3,4].

Some of these studies use clinical recorded electrograms using different electrogram arrays with different electrode sizes that are successively positioned on similar locations on the atria. However, it should be noted that not all observed changes in the electrogram properties are due to changes in electrode size, but also due to the spatio-temporal varying nature of electrical wave propagation (specially during AF) and the changes in the inter-electrode distances. Moreover, bipolar electrograms are also affected by varying propagation directions. In this study, we exclusively investigate the effect of the electrode size on the properties of high resolution unipolar electrogram arrays by keeping the other parameters like inter-electrode distances and electrical wave propagation patterns fixed. We use both clinical observation and electrophysiological models that govern the wave propagation and electrogram generation to analyze and investigate these effects. This is done by investigating the electrode's transfer function and its properties, making the comparisons and conclusions more robust. Moreover, we investigate these results for tissues with different levels of inhomogeneity in the conductivity map. We also focus on the overall properties of the electrogram array and not only on the per-electrode features. These include the overall error in local activation time estimation, length of slow conduction or block lines, low voltage areas in the tissue, as well as the number of deflections.

We first present the electrogram model, our approach for generating simulated electrograms, and our proposed framework for generating high resolution electrogram arrays with different electrode sizes from clinical electrograms in Section 2. We also provide a description of our clinical recording setup and employed measures for characterizing the electrogram array properties in the same section. In Section 3 and Section 4, we perform our approach on simulated and clinical electrograms, respectively, and present the final results. We also discuss the optimal electrode diameter and appropriate inter-electrode distances for electrode arrays with different electrode sizes, the maximum electrode size for capturing scarred tissue of different sizes, and a proper scaling of the electrogram amplitude for a better comparison of electrograms recorded with different arrays. We discuss our findings and conclude the study in Section 5.

2. Method

2.1. Atrial tissue computer model

In our model we consider the atrial tissue as a two dimensional mono-layer grid of cells where the electrode array is positioned at a constant height z_0 above the atrial tissue. We model the electrogram as a weighted summation of *trans*-membrane currents produced by the cells in the tissue in the vicinity of the electrode, where the weights depend on the inverse of the cell-to-electrode distances. An electrogram at location (x, y) and at time sample t can then be modeled as [13].

$$\varphi(x_m, y_m, t) = \frac{1}{4\pi\sigma_e} \int_{\mathscr{A}} \frac{I_{\text{tr}}(x, y, t)}{\sqrt{(x - x_m)^2 + (y - y_m)^2 + z_0^2}} dA(x, y), \tag{1}$$

where $m = 1, 2, \cdots, M$ is the electrode index with M the total number of electrodes, $I_{\text{tr}}(x, y, t)$ is the *trans*-membrane current, $\mathscr{A}$ is the area in which the modeled cells are located, $A(x, y)$ is the area variable, and σ_e is the constant extra-cellular conductivity. Note that for now we assume that we are recording the electrograms with point electrodes whose diameters can be neglected. We will investigate the effect of electrode diameter later in Section 2.2.

The transmembrane current produced by each cell can be computed

using the following equation [14].

$$I_{\text{tr}}(x, y, t) = S_v^{-1} \nabla \cdot \mathbf{\Sigma}(x, y) \nabla V(x, y, t), \tag{2}$$

where $V(x, y, t)$ is the per cell potential, $\mathbf{\Sigma}(x, y)$ is the intracellular conductivity tensor, and $S_v = 0.24\mu\text{m}^{-1}$ is the cellular surface-to-volume ratio. The potential and *trans*-membrane current can simultaneously be calculated using the reaction-diffusion equation that governs the action potential propagation in the tissue [14],

$$C \frac{\partial V(x, y, t)}{\partial t} = I_{\text{tr}}(x, y, t) + I_{\text{st}}(x, y, t) - I_{\text{ion}}(x, y, t, V), \tag{3}$$

where $C = 1\mu\text{Fcm}^{-2}$ is the total membrane capacitance, I_{st} is the stimulus current, and I_{ion} is the total ionic current computed according to the Courtemanche model in Ref. [15].

2.2. Electrode's transfer function model

For a uniform grid of cells with Δx denoting the cell-to-cell distance, we can rewrite Eq. (1) as a 2D spatial convolution of transmembrane currents with an appropriate electrode transfer function $R_0(x, y)$ as

$$\varphi(x, y, t) = c\, S_0(x, y) (R_0(x, y) ** I_{\text{tr}}(x, y, t)), \tag{4}$$

where $**$ denotes the 2D spatial convolution, and $c = \Delta x^2 / 4\pi\sigma_e$ contains all constants and will be omitted for simplification. We introduced in Eq. (4) the sampling operator $S_0(x, y) = \sum_m \delta(x - x_m, y - y_m)$ with Dirac delta functions to select the M spatial locations on the grid on which we have measurements and replace the other locations with zero. This can also be used to de-select faulty electrodes. The electrode transfer function is

$$R_0(r) = \frac{1}{\sqrt{r^2 + z_0^2}}. \tag{5}$$

where $r = \sqrt{x^2 + y^2}$ is the horizontal distance between the electrode (at origin) and a cell at location (x, y). However, an electrode whose diameter is bigger than the modeled cell size (i.e., $d_0 > \Delta x$) can no longer be considered as a point electrode. The transfer function should therefore take the diameter of the electrode into account as proposed in Ref. [8], i.e.,

$$R_{d_0}(r) = 2\arcsin \frac{d_0}{\sqrt{(r - d_0/2)^2 + z_0^2} + \sqrt{(r + d_0/2)^2 + z_0^2}}. \tag{6}$$

The first row of Fig. 1 shows the 2D representation of the electrode normalized transfer function of a point electrode from Eq. (5) as a function of x and y, as well as the normalized transfer function based on r, both computed by setting $z_0 = 0.5$ mm. As can be seen, the value of the transfer function, or the weight of the *trans*-membrane current in Eq. (4), for the cell that is exactly under the electrode's center equals to 1. A large weight indicates more influence on the final recorded electrogram. As we move further from the center, the weights decrease but the values are still noticeable. One important parameter commonly used to characterize the transfer function is the full width at half maximum (FWHM), denoted on the plot. It shows the diameter at which the weight of the cells is greater than half of the maximum value, indicating their significant influence on the final recorded electrogram. A small FWHM (a narrower transfer function) denotes that the electrode records data from a smaller area thus providing more local electrograms. However a large FWHM denotes that the recorded electrogram will be the summation of activities in a larger area. This can severely affect the morphology of the local activities if the propagation is not homogeneous in the electrode's neighborhood. In general, summing up activities in a larger area will smooth out the important local details.

The bottom left plot in Fig. 1 shows the transfer functions for different electrode diameters $d_0 \in 0.5, 2, 4, 8$ mm with $z_0 = 0.5$ mm. The
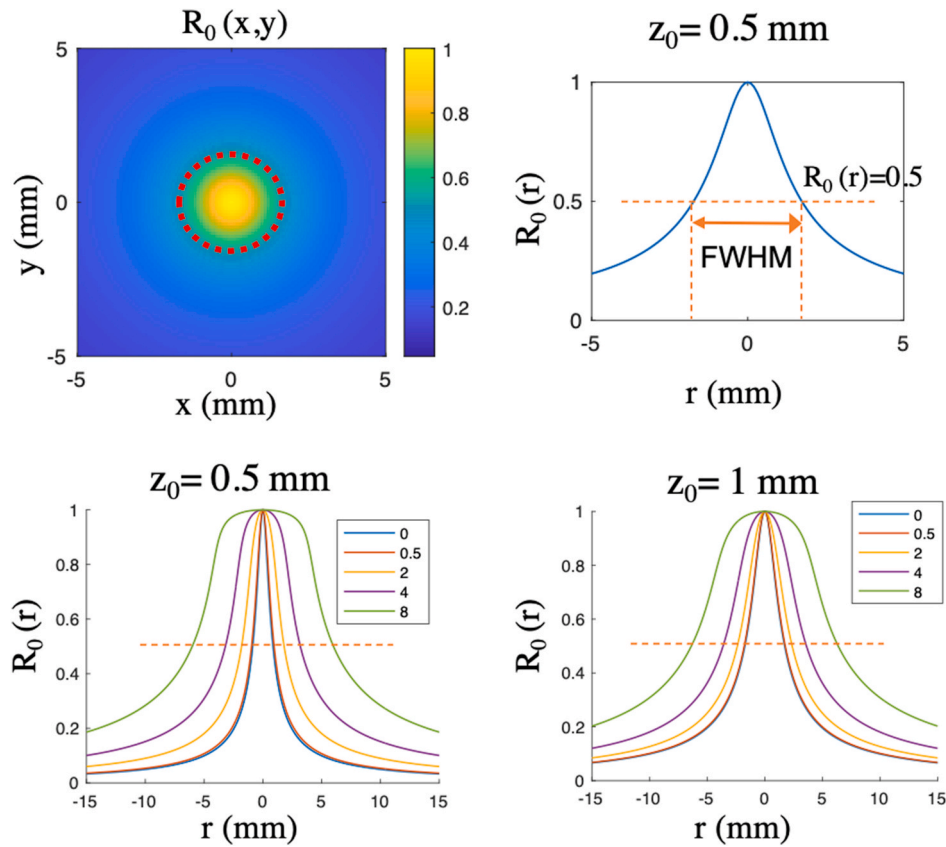
Fig. 1. Top left: the 2D representation of the electrode normalized transfer function $R_0(x,y)$ of a point electrode. The red dashed circle represents the FWHM. Top right: the electrode transfer function based on $R_0(r)$. Bottom: $R_{d_0}(r)$ for different electrode diameters $d_0 \in 0, 0.5, 2, 4, 8$ mm with $z_0 = 0.5$ mm (left) and $z_0 = 1$ mm (right).

bottom right plot in Fig. 1, also shows the transfer functions when $z_0 = 1$ mm, assuming a thicker tissue. As can be seen in both plots, as the electrode diameter increases, the transfer function gets wider (larger FWHM) indicating that the recorded electrogram will be more influenced by the neighboring activities. The difference in FWHM is more evident in thinner tissues and for smaller diameters. This will be investigated in more detail in Section 3.3.

2.3. Modeling abnormal tissue

To generate simulated fractionated electrograms that are representative for clinical data, various approaches have been suggested in literature. Jacquemet et al. in Ref. [8] incorporate the heterogeneities in the conductivity as a set of randomly positioned lines of conduction block that disconnect the coupling between the cells on the grid. However, Vigmond et al. in Ref. [16] model the conduction disturbance by randomly disconnecting the coupling between some modeled cells and their neighbors through randomly positioned dots of conduction block. In this study we use both patterns simultaneously for simulated conductivity maps of modeled tissue. This provides simulated electrograms and activation maps that are more similar to clinical recordings (by visual inspection).

To simulate electrograms with different levels of fractionation, we use conductivity maps with varied levels of conduction block density. These are shown in the first row of Fig. 2 denoted as T1, T2 and T3 having a low, medium and high density of conduction block, respectively. For comparison, we have also shown the results for a homogeneous tissue with planar wave propagation, denoted by T0, which serves as a standard reference for other tissue types. The size of each tissue is 213×173 cells, with a cell-to-cell distance of $\Delta x = 0.5$ mm. We also activate the tissues using one or two activation waves entering the tissue

from different locations to simulate the activation maps during AF.

To model action potential propagation in the simulated tissues, Eq. (3) is discretized and solved using a finite difference method with no flux boundary condition. The activities are simulated for 1000 ms to include one complete atrial beat, but only a selected time window of 150 ms in length is used for evaluation of electrograms as it includes all the atrial activities. A more detailed description of the simulation steps and parameters can be found in Ref. [17]. The resulting activation maps are shown in the second row of Fig. 2. Each pixel in the activation map represents the true activation time of its corresponding cell which is annotated as the time when the cell's potential V reaches a threshold value of -40 mV in the depolarization phase of its action potential. The white pixels belong to the cells that were positioned on a conduction block and did not get activated. Finally, Eq. (1) is used to compute the simulated electrograms recorded by an assumed electrode array of size 77×33 cells positioned on the center of the tissue at a constant height of $z_0 = 0.5$ mm, which is denoted by a red rectangle on the maps. The last panels in Fig. 2 show example electrograms from each tissue computed for four different electrode diameters $d_0 \in 0.5, 2, 4, 8$ mm.

2.4. Clinical studies

The study population consisted of 10 adult patients undergoing surgery in the Erasmus Medical Center Rotterdam. This study was approved by the institutional medical ethical committee (MEC2010-054/MEC2014-393) [18,19]. Written informed consent was obtained from all patients. Patient characteristics (e.g. age, medical history, cardiovascular risk factors) were obtained from the patient's medical record. Epicardial high-resolution mapping was performed prior to commencement to extra-corporal circulation, as previously described in detail [20]. A temporal bipolar epicardial pacemaker wire attached to
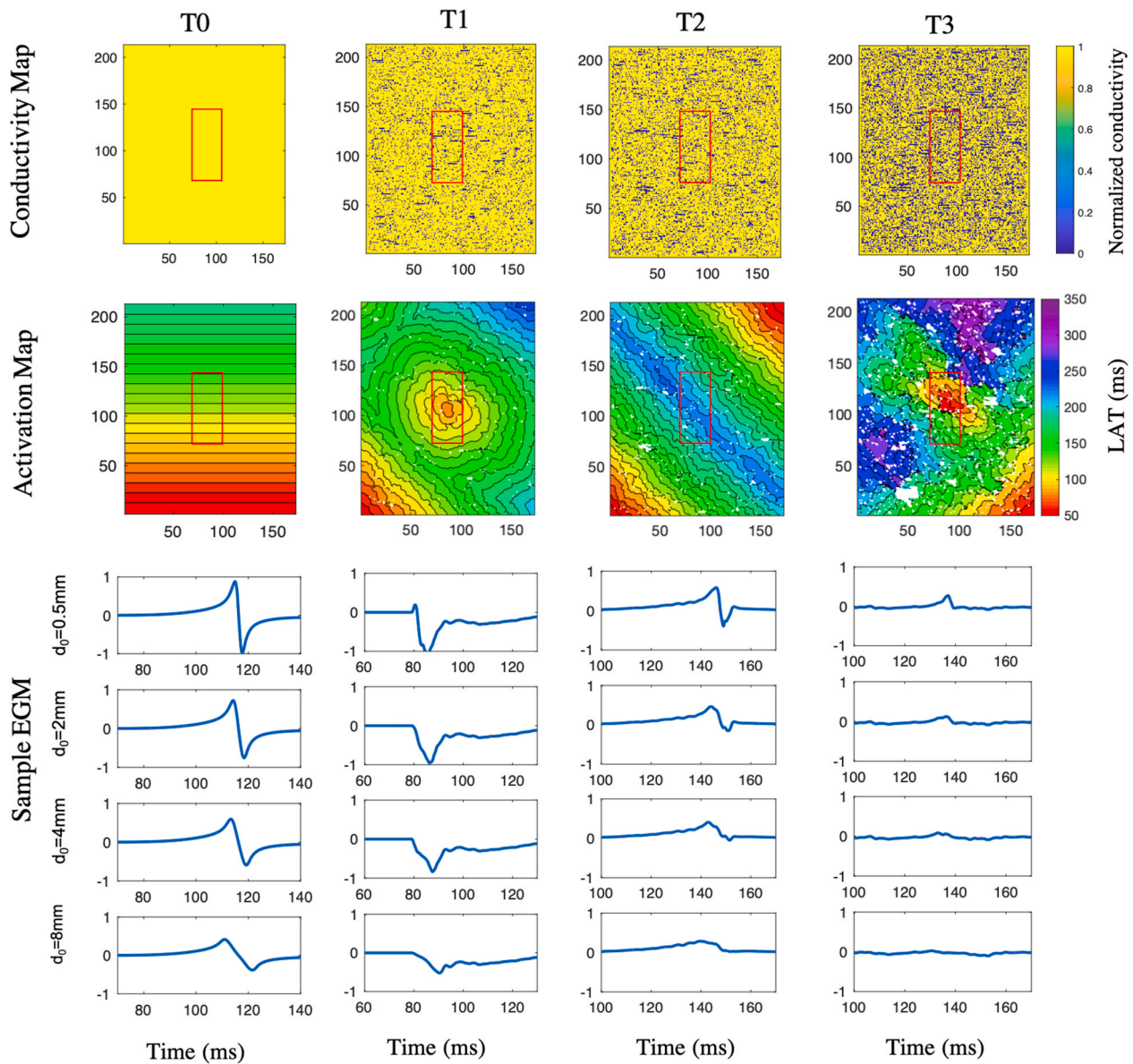
Fig. 2. Conductivity map, activation map and an example electrogram simulated for different electrode sizes of four simulated tissues. T0 is modeled as a homogeneous tissue while T1, T2 and T3 have a low, medium and high density of conduction block in their conductivity map, respectively. The red rectangle represents the electrode array position. We assume there is one electrode on top of each modeled cell.

the RA free wall served as a reference electrode. A steel wire fixed to subcutaneous tissue of the thoracic cavity was used as an indifferent electrode. Epicardial mapping was performed with a 192-electrode array (electrode diameter 0.45 mm, inter-electrode distances 2.0 mm). The electrode array is subsequently positioned visually by the surgeon on 9 mapping atrial sites using the anatomical borders. We only use the data recorded from Bachmann's bundle. Ten seconds of induced AF were recorded from every mapping site, including a surface ECG lead, a calibration signal of 2 mV and 1000 ms, a bipolar reference EGM and all unipolar epicardial EGMs. Data was stored on a hard disk after amplification (gain 1000), filtering (bandwidth 0.5 to 400 Hz), sampling (1kHz) and analogue to digital conversion (16 bits).

2.4.1. Interpolating (clinical) electrograms and estimating electrograms for different electrode sizes

Due to the unstable and unpredictable nature of electrical wave propagation during AF, it is not possible to repeat similar recordings with different electrode arrays (having different electrode diameters and

therefore different inter-electrode distances) during AF. To overcome this issue and to interpolate and estimate the electrograms recorded with different arrays, we first estimate high resolution transmembrane currents and subsequently model the effect of larger electrode dimensions. We discretize the 3D tissue activity in space. We use source clamping and replace each block of cells in the real three dimensional tissue with a modeled "cell" on a uniform 2D grid of cells similar to the simulated data. Next, we estimate the high resolution transmembrane currents using Eq. (4) and the recorded electrograms. This can be done by solving the following regularized optimization problem as suggested in Ref. [21].

$$\min_{I} \quad \| \varphi - S_0(R_0 ** I) \|_2^2 \; + \; \lambda \parallel I' \parallel_1 \tag{7}$$

where

$$\|I\|_2^2 := \sum_x \sum_y \sum_t \left| I\left[x,y,t\right] \right|^2, \quad \|I'\|_1 := \sum_x \sum_y \sum_t \left| I'\left[x,y,t\right] \right|$$

and where λ is the regularization parameter. Employing the ℓ_1-norm regularization function (i.e., $\| . \|_1$) helps to preserve the main features of the transmembrane currents among which sparse fast temporal changes (deflections). These are of high importance for correct LAT estimation. More details on an efficient approach to solve Eq. (7) can be found in Ref. [22]. After estimating the high resolution *trans*-membrane current, we can estimate different electrograms for varying electrode sizes and inter-electrode distances using Eq. (4) with an appropriate transfer function from Eq. (6).

2.5. Electrogram analysis

Here, we introduce four measures that are used to characterize the properties of the electrogram arrays. Notice that both simulated and clinical electrograms' amplitudes are scaled with a constant value so that the amplitude of the electrograms of a homogeneous wave propagating through the tissue (as in tissue type T0) recorded by the smallest electrode ($d_0 = 0.5$ mm) equals 1 V. The scaling value is different for clinical and simulated recordings but similar for different electrode sizes. We characterize the properties of the simulated and clinical high resolution electrogram arrays recorded during one atrial beat using the following four measures:

1. **LATE**: percentage of large absolute errors in LAT estimation denoted by LATE. These are the error values that are larger than 10 ms. This measure is only evaluated for simulated tissue where we have access to true activation times. The true activation time is annotated as the time when the potential of the cell that is exactly under the electrode reaches the value of -40 mV, insuring that the action potential is triggered. The estimated activation time of the simulated electrogram is annotated as the point with the steepest descent. The threshold value of 10 ms was selected heuristically. However different threshold values yield a similar pattern of changes.

2. **LSC/B**: length of lines of slow conduction or block in the tissue denoted by LSC/B. To compute this value we first find the delay between each cell and its four direct neighbors on the grid of cells. If the delay is bigger that 0.7 ms it will be considered as a slow conduction or block with the length of Δx. This threshold value is selected with respect to the standard delay between neighboring cells estimated from the standard tissue T0. Note that this is not a small threshold considering the cell-to-cell distances of $\Delta x = 0.5$ mm in the simulation. Moreover, since we model inhomogeneity in the tissue using dots and small lines of block, their effects on the LAT also ranges from very small to large values. Fig. 3 (b) shows an example activation map with its lines of slow conduction or block denoted by thick black lines.

3. **LVA**: percentage of electrograms with lower peak-to-peak voltage than 0.2 V denoted by LVA. The peak-to-peak voltage is defined as the difference between the maximum and the minimum electrogram amplitude and is shown in an example electrogram in Fig. 3 (a). The

threshold value was selected heuristically, making sure it is small enough to indicate the changes in between different tissue types and electrode diameters.

4. **ND, SD, and MD**: percentage of electrograms having no deflection (ND), a single deflection (SD), or multiple deflections (MD). We only count the deflections having a smaller average slope than -0.02 V/ms. The threshold value was selected heuristically to avoid small negligible deflections caused by noise and artifacts. Fig. 3 (b) shows an example electrogram with 2 deflections.

It is important to note that all the measures are evaluated for high resolution electrogram arrays assuming that there is one electrode on top of each cell. This is not possible in practice because the inter-electrode distance should be larger than the electrode diameter. However, the results will confirm that the changes in the measures are due to the changes in the electrode's size and not due to the different inter-electrode distances. The above mentioned measures are computed using custom written MATLAB codes.

3. Simulation results

3.1. Effect of electrode size on electrogram properties

In this section, we investigate the effect of the electrode size on the properties of the simulated electrograms using the measures we introduced in Section 2.5. Five randomly generated conductivity maps were modeled for each tissue type T1 to T3, which were previously shown in Fig. 2. The tissues were stimulated with one or two activation waves entering the tissue from different locations and the resulting electrograms were computed for four different electrode diameters $d_0 \in 0.5, 2, 4, 8$ mm. The last row of Fig. 2 shows an example electrogram from each tissue computed for the four different electrode diameters. For a better comparison, Fig. 4 also shows simulated electrograms for
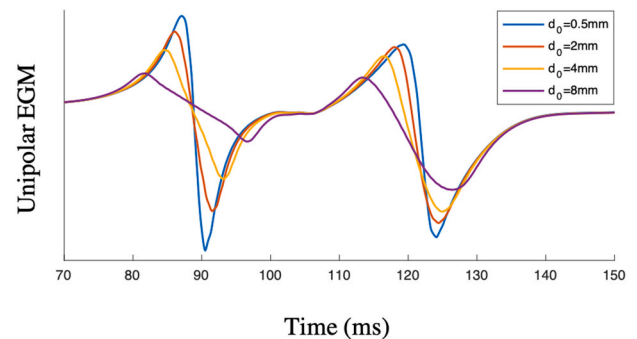
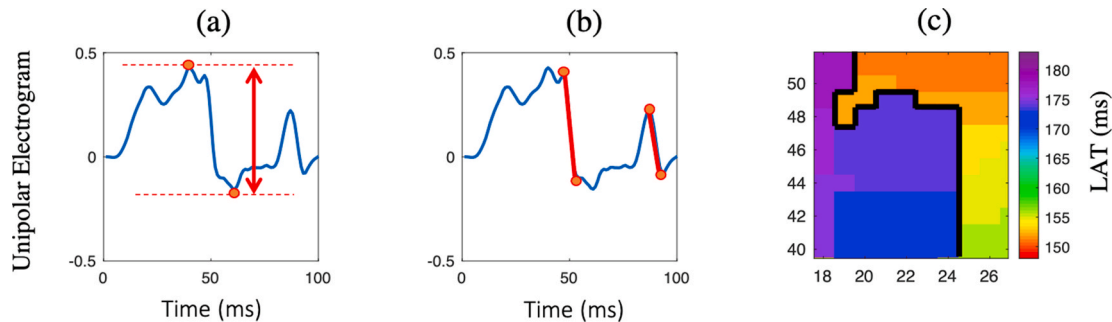**Fig. 4.** An example of a simulated atrial activity recorded by different electrode sizes.

Fig. 3. (a) Unipolar electrogram with the peak-to-peak voltage denoted by the red two-sided arrow. If the peak-to-peak voltage is smaller than 0.2 V, the EGM will be counted as a low voltage electrogram. (b) Unipolar electrogram from (a) with two of its deflections (downward slopes) denoted by red lines. As can be seen there are more deflections in the signal but we only count those with an average slope that is smaller than -0.02 V/ms. (c) Example activation map (a segment of T7 in Fig. 10) with the lines of block denoted by black lines. These are the areas between two neighboring cells with delays in LAT that are larger than 0.7 ms.

different electrode sizes in one plot. These electrograms belong to T5 in Fig. 5 with two distinct deflections as a result of a long line of block (for more details see Section 3.4).

The measures introduced in Section 2.5 were evaluated for all 2541 × 5 = 12705 simulated electrograms of each tissue type (77× 33 = 2541 electrograms per map) and are presented in Tables 1–4. As can be seen in the resulting tables, increasing the electrode size increases the error in LAT estimation while the length of detected slow conduction or block lines in the tissue decreases. Except for the homogeneous tissue T0, where using bigger electrode diameters results in an increase in LSC/B which is almost similar for all electrode diameters. As a result, the final activation maps seem smoother. This will be discussed in more detail in Section 3.2.

The percentage of low voltage areas in the tissue also increases by increasing the electrode size, indicating that using bigger electrodes decreases the amplitudes of recorded electrograms. However, by comparing the results of lower voltage areas in Tables 1–4, it seems that a larger diameter is more useful at indicating the differences in low voltage areas of different tissue types and respectively the mean conductivity of the underlying substrate, even if the discrete block lines in the simulation are missed.

The percentage of single and multiple deflections in the electrograms decreases by increasing the diameter. This is because the slope of some of the deflections gets very small and it will not be annotated as a deflection anymore.

However, as can be seen in the tables, the variations in electrogram properties caused by using different electrode diameters are more evident in tissues with higher level of heterogeneity or more scarred tissues. This also indicates that electrograms generated in homogeneous tissues will not be much affected by the electrode diameter.

3.2. Effect of electrode size on the activation map

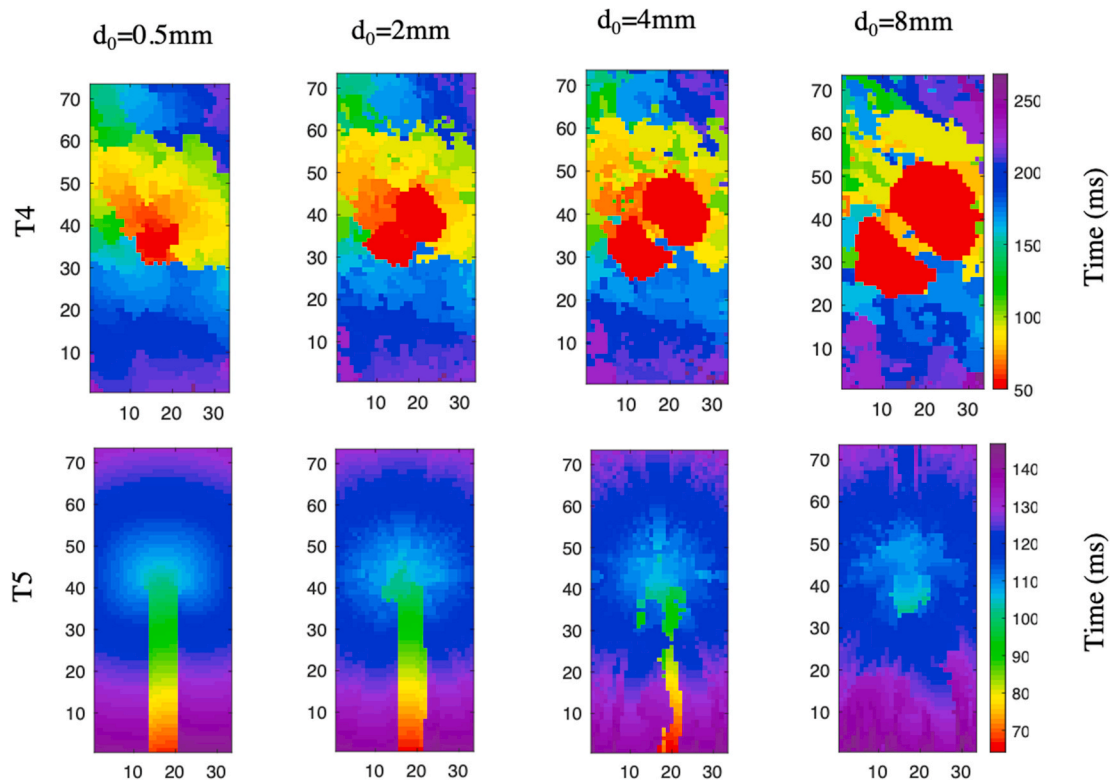We use some examples to visualize the effect of electrode size on the resulting activation maps. As discussed earlier in Section 3.1, using bigger electrode sizes increases the error in LAT estimation and decreases the length of detected conduction block lines. This happens

Table 1
Measures evaluated for $m = 77 \times 33$ EGMs of tissue type T0.

d0 (mm)	Late %	LSC/B (cm)	LVA %	No. Deflections %		
				ND	SD	MD
0.5	0	0	0	0	100	0
2	0	46.2	0	0	100	0
4	0	41.25	0	100	0	0
8	0	44.55	0	100	0	0

Table 2
Measures evaluated for $m = 77 \times 33 \times 5$ EGMs of tissue type T1.

d0 (mm)	Late %	LSC/B (cm)	LVA %	No. Deflections %		
				ND	SD	MD
0.5	0.97	86.15	0	0.97	70.70	28.32
2	2.36	80.18	0.07	98.09	1.90	0
4	5.23	79.37	0.90	99.26	0.73	0
8	18.79	66.10	25.42	100	0	0

Table 3
Measures evaluated for $m = 77 \times 33 \times 5$ EGMs of tissue type T2.

d0 (mm)	Late %	LSC/B (cm)	LVA %	No. Deflections %		
				ND	SD	MD
0.5	2.35	98.24	0	2.30	65.54	32.14
2	6.07	85.11	0.72	98.64	1.35	0
4	12.61	82.63	7.41	99.39	0.60	0
8	38.57	68.35	71.54	100	0	0

Fig. 5. Activation map estimated from high resolution electrogram arrays with different electrode sizes. T4 has the same tissue conductivity pattern as T2 and in T5 two lines of block are positioned along the center of the tissue.

Table 4
Measures evaluated for $m = 77 \times 33 \times 5$ EGMs of tissue type T3.

d0 (mm)	Late %	LSC/B (cm)	LVA %	No. Deflections %		
				ND	SD	MD
0.5	11.19	115.03	0.32	10.01	62.19	27.79
2	32.61	94.06	17.35	97.99	2.00	0
4	49.34	84.16	65.09	98.58	1.41	0
8	72.19	65.44	99.28	99.89	0.10	0

because the electrograms recorded by bigger electrodes are affected more by neighboring activities. Therefore, the deflection generated by larger and stronger inhomogeneous waves in the neighborhood may over-impose the small, but main, local deflections. As a result, the final activation maps seem smoother and more homogeneous.

Fig. 4 shows an example of a simulated atrial activity recorded by different electrode sizes. As can be seen, two deflections are visible in each activity. The first deflection (at 90 ms) belongs to the local main activity and the second deflection (at 123 ms) belongs to a strong neighboring activity. As the electrode size increases, the second deflection gets steeper compared to the first deflection. Annotating the steepest descent as the LAT will then result in annotating the second deflection for electrode of diameters $d_0 = 4$ mm and 8 mm. That is an absolute error of about 33 ms in LAT estimation.

Fig. 5 shows estimated activation maps of two simulated tissues recorded by electrode arrays having different electrode sizes. These examples imitate the two patterns of common changes that we observed in clinical cases. T4 has the same tissue conductivity pattern as T2 (medium density of conduction blocks) with a different stimulation pattern (explained in Section 2.3) resulting in generation of complex fractionated atrial electrograms. As can be seen, small waves in the tissue are over-imposed by larger and stronger activities in their surrounding and the smooth variations from one color to another are replaced by sharp variations. In T5 (second row of Fig. 5) two lines of block are positioned along the center of the tissue. The activation map starts from the area in-between these lines and then propagates through the whole tissue. As can be seen, this abnormal area is completely lost when we use bigger electrode sizes. As mentioned before, this happens because the activities generated in this abnormal area have lower amplitude compared to the stronger activities outside the block lines and an electrode with a bigger size records more activities from its neighborhood. We discuss this case in more detail in Section 3.4.

3.3. Optimal electrode diameter and inter-electrode distance

The electrode transfer function in Eq. (6) and shown in Fig. 1 can be used for calculating the optimal electrode diameter and inter-electrode distance. This can be done by investigating the FWHM of different electrode diameters. Fig. 6 shows the calculated FWHM as a function of
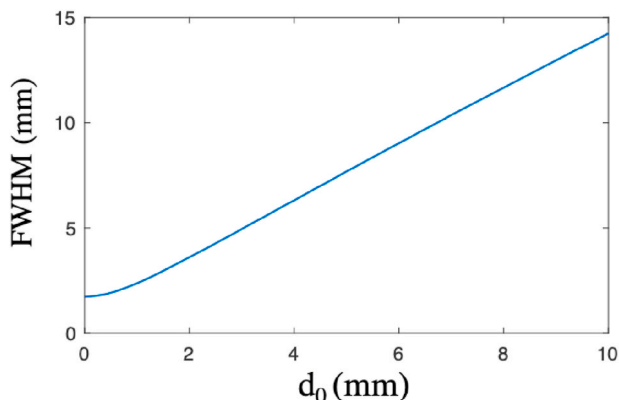
the electrode's diameter (with $z_0 = 0.5$ mm). This plot has two important features. First, even for a point electrode, FWHM= 1.73 mm is nonzero. Secondly, FWHM is almost constant for small diameters and the curve bends around $d_0 = 0.5$ mm. These observations can lead to two important conclusions:

(i) Optimal electrode diameter: an optimal electrode diameter is around $d_0 = 0.5$ mm. This is the largest value with a similar FWHM to a point electrode. Note that smaller electrodes are affected more by noise so there is a trade off between high SNR and small FWHM. Therefore, it is also not preferred to use the smallest electrode possible.

(ii) Optimal inter-electrode distance (in order to capture all the spatial information of the electrical activities in the tissue): To find this parameter, we first need to estimate the maximum spatial frequency that is presented in electrical activities. This can be a quite complicated task due to the three dimensional inhomogeneous structure of the atrial tissue and the complex unstable wave propagation patterns. On the other hand, no matter how high these spatial frequencies are, they will eventually be recorded by surface electrodes which inherently perform as a spatial low-pass filter. As shown in Ref. [22], the FWHM discussed in Section 2.2 can be also used as a short-hand measure of the appropriate inter-electrode distance. As an example for an electrode with $d_0 = 0.5$ mm, we suggest an optimal inter-electrode distance of around 1.9 mm, which is equal to its FWHM at $z_0 = 0.5$ mm.

Fig. 7 shows the FWHM as a function of both d_0 and z_0. As can be seen in this figure, as the electrode diameter or the electrode height (or equivalently tissue thickness) increases, the required inter-electrode distance also increases. This means that FWHM and the low-pass filtering effect of the electrode increases. This will result in losing spatial information by electrodes. Even putting them closer to each other in an array will not compensate that loss. Therefore, we can effectively use larger inter-electrode distances. Conversely, electrodes with smaller diameters have smaller FWHM and can potentially capture spatial information with higher frequencies and by putting these electrodes closer to each other on an array, we can record this information.
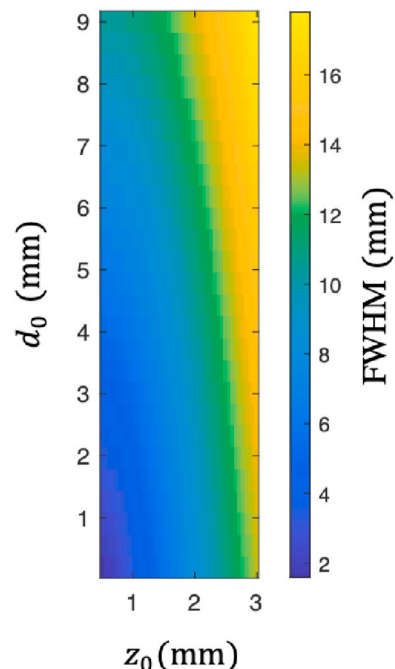

Fig. 6. FWHM calculated for different electrode diameters with $z_0 = 0.5$ mm.

Fig. 7. The estimated FWHM for different values of d_0 and z_0.

3.4. Maximum electrode size for recording scarred tissue

In this section, we perform an experiment to investigate the maximum electrode size for the detection of abnormal areas and conduction block lines using simulated tissue. We use the same pattern as in T5 in Fig. 5 for the scarred tissue where two lines of conduction block are positioned along the center of the tissue with a distance of L_{block}. The activation wave starts from the area in between these lines and then propagates through the whole tissue. As can be seen in T5, this abnormal area is completely lost when we use bigger electrode sizes. As mentioned before, this happens because the activities generated in this abnormal area have lower amplitude compared to the stronger activities outside the block lines and an electrode with a bigger size records more activities from its neighborhood. We increased the distance between the two parallel lines of blocks and visually inspect the activation map estimated from different electrode arrays to determine the maximum electrode diameter $d_{0,max}$ that can still provide some evidence of the abnormality in the tissue. The results can be seen in Fig. 8. As an example, the two block lines in T5 are distanced at $L_{block} = 3.5$ mm, and, as can be seen in Fig. 8, the maximum electrode diameter that can still provide an evidence of this abnormality is around 4.2 mm. Notice that this is a simple example compared to complex clinical cases where the results are affected by many underlying parameters of the tissue.

4. Clinical results

As discussed in Section 2.4.1, due to the unstable and unpredictable nature of electrical wave propagation during AF, it is not possible to repeat similar clinical recordings with different electrode arrays. Therefore, to model these recordings, we use our approached presented in Section 2.4.1 to first estimate high resolution transmembrane currents and then use them to interpolate and calculate electrograms with bigger electrode sizes. The methodology used for estimation of *trans*-membrane current is discussed and evaluated in Ref. [22]. Here, to evaluate its performance in reproducing the electrograms, we find the mean correlation coefficient between the real clinical electrograms and their simulated electrograms after finding the *trans*-membrane currents and recalculating the electrograms. The mean correlation coefficient is equal to 0.97 ± 0.004 (mean $\pm$ standard deviation) which indicates a good simulation. Note that we can only calculate this measure for the low resolution 24×8 clinical electrograms and for $d_0 = 0.5$ mm, as we do not have the ground-truth EGMs for bigger electrode sizes or higher resolutions. Fig. 9 shows four neighboring clinical (real) EGMs and the
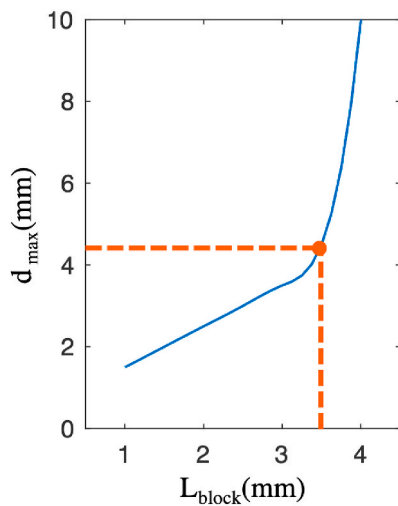

Fig. 9. Real (in orange) and interpolated electrograms (in blue) for clinical recordings with $d_0 = 0.5mm$. Note that for an easier inspection, only electrograms from dark blue electrodes have been shown.

interpolated electrograms in between them.

4.1. Statistical analysis

A similar analysis as in Section 3.1 was performed on 10 clinical electrogram arrays of size 24×8 recorded from Bachmann's bundle for 10 different patients. The signals were recorded for 10 s during induced AF resulting in fractionated electrograms with various levels of fractionation. Note that the electrograms were initially interpolated and modeled for different electrode sizes. This resulted in $24 \times 8 \times 4$ electrograms in total. The measures introduced in Section 2.5 were evaluated for one atrial beat of length 150 ms (visually selected to make sure each electrogram contained atrial activity) and are presented in Table 5. We did not present the result for the error in LAT estimation because we do not have access to the true values in clinical data. As can be seen in the table, the changes in the properties of electrograms recorded by different electrodes follows the same pattern as for the simulated data.

Fig. 8. Maximum electrode diameter $d_{0,max}$ for recording a visible scarred tissue, as a function of L_{block} which denotes the distance between two lines of block.
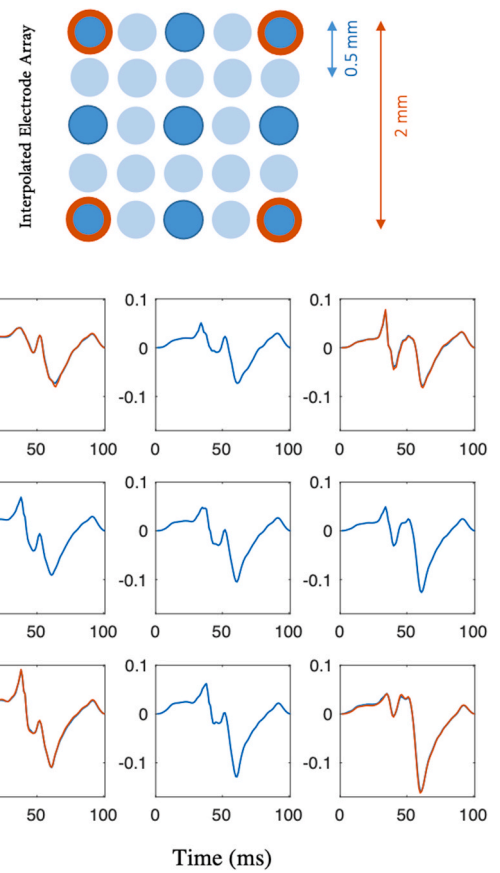
Table 5
Measures evaluated for $24 \times 8 \times 4^2 \times 10$ interpolated clinical electrograms recorded from Bachmann's bundle.

d0 (mm)	LSC/B (cm)	LVA %	No. Deflections %		
			ND	SD	MD
0.5	80.34	47.38	71.31	25.56	3.12
2	68.47	53.13	77.72	20.99	1.27
4	59.95	60.28	84.25	15.62	0.12
8	56.09	78.40	93.46	6.52	0.00

4.2. Changes in activation maps

Similar patterns as in Section 3.2 are also seen in the clinical data. Fig. 10 shows two examples of how the high resolution activation maps change by using different electrode sizes. As expected, the small deflections and small wavelets in T6 are over-imposed by larger and stronger activities in their surrounding area as the electrode size increases. This leads to a decrease at the total number of wavelets in the area. T7 also shows an example where the abnormal area with long delays in the activation map is partly or completely missed due to the increase in the electrode size.

4.3. Scaling electrograms' amplitude

A proper scaling of the electrograms' amplitudes recorded with different electrode sizes can to some extent compensate for differences in the measures that characterize the electrograms. We propose to use the ratio between the norm of the transfer functions of the electrodes for scaling their amplitudes for a better comparison of their recorded electrograms. This can be formulated as

$$\widehat{\varphi}_{d_0}(x_m, y_m, t) = \frac{\|R_0(r)\|_2}{\|R_{d_0}(r)\|_2} \varphi_{d_0}(x_m, y_m, t) \tag{8}$$

where $R_0(r)$ and $R_{d_0}(r)$ are calculated from Eqs. (5) and (6), $\widehat{\varphi}$ is the scaled electrogram, and $\| \cdot \|_2$ is the Euclidean norm or $l2$-norm. This will make the measures like LVA and the number of deflections, more invariant to the electrode's diameter. However, it will not affect the

estimation of LATs, or any parameter that is extracted from it like LSC/B.

Table 6 shows the new measures (cf. the non-scaled version in Table 5) after using the norm of the distance kernel for scaling the data. Notice that approaches like the maximum amplitude or steepness of the recorded electrograms for scaling or normalizing them are realization based and thus less stable. Such parameters will depend on the propagation patterns and are prone to spatial and temporal variations, making the results incomparable and not generalizable.

5. Discussion and conclusion

In this paper, we studied the effect of electrode size on the properties of the recorded electrograms. We started by simulated electrograms of 2D atrial tissues and present the effect of different electrode sizes on electrogram properties including the error in LAT estimation, the length of slow conduction or blocks (LSC/B) observed on the resulting activation map, percentage of observed low voltage areas (LVA), and the

Table 6
Measures evaluated for $24 \times 8 \times 4^2 \times 10$ interpolated clinical electrograms recorded from Bachmann's bundle after scaling the electrograms.

d0 (mm)	LSC/B (cm)	LVA %	No. Deflections %		
			ND	SD	MD
0.5	80.34	47.38	71.31	25.56	3.12
2	68.47	46.62	74.11	24.13	1.75
4	59.95	47.67	77.20	22.19	0.59
8	56.09	52.40	82.41	17.47	0.10
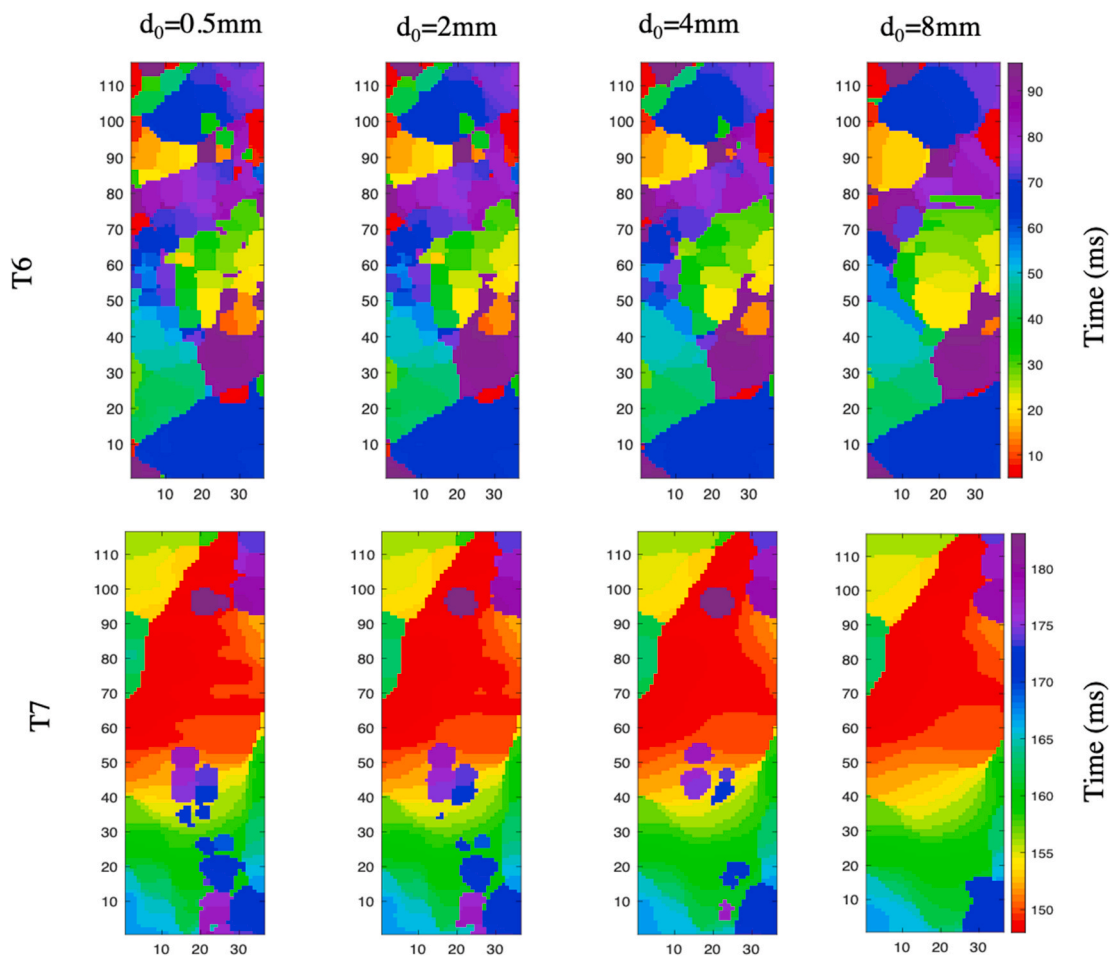
Fig. 10. Example activation maps estimated from high resolution electrogram arrays with different electrode sizes, estimated from clinically recorded electrogram arrays.

number of deflections in the recorded electrograms. The results were then tested on clinical electrograms of 10 patients recorded from Bachmann's bundle. Since we had no access to the recorded electrograms recorded with different electrode diameters, we first estimated the high resolution transmembrane current maps using the approach in Ref. [22] and then used the currents and the electrode transfer function to generate such recordings. The results were comparable to those of simulated data.

The results show that using bigger electrodes produces larger error in LAT estimation, which is in accordance with previous results shown in a previous study [10]. These errors in LAT estimation will result in the estimation of a smoother activation map than the true map. These results were also observed in experiments on clinical bipolar electrograms in Refs. [3,5].

The electrograms recorded with a bigger electrode size are in general smoother with smaller slopes and smaller peak-to-peak voltages. Some of the deflections in these signals are so smooth that they are not annotated as a deflection in the recording. This will result in an increase in low voltage areas in the tissue, which agrees with the result of previous studies in Refs. [6,8]. However, if there is no recording with a smaller electrode available for setting the proper thresholds, one might use smaller threshold values for detecting such deflections. This can result in detecting more deflections. This can explain why some studies such as [7–9] suggest that increasing the electrode size increases the fractionation level in the tissue.

However, by comparing the results of lower voltage areas in Tables 1–4, it seems that a larger diameter is more useful at indicating the difference in low voltage areas in between different tissue types with different inhomogeneity levels. Considering that in the inhomogeneous cardiac tissue, lower conductivity also means lower voltage in that area, we can conclude that bigger electrodes are more useful at indicating the mean conductivity of the underlying substrate, even if the discrete slow conduction or block lines in the activation map are missed.

Although these conclusions have been partly discussed or hinted in previous studies, in the current study, we focused on a more systematic approach towards them. By employing the electrophysiological models and the electrode's transfer function, we could analyze and discuss these effects in more depth. Moreover, the introduced approach for interpolating and modeling clinical electrograms with different electrode sizes allowed us to investigate these effects for recordings of similar wave propagation patterns. It also enabled us to only focused on the electrode's diameter and not the inter-electrode distances.

Moreover, we discussed the effect of the optimal electrode diameter and the required inter-electrode distances (or the array resolution) for capturing all the possible spatial information. We performed an experiment to investigate the required minimum electrode size for capturing an inhomogeneous activity in between two parallel block lines in the tissue. We also introduced a proper way for scaling electrograms with different electrode's diameter for a better comparison.

These results show the importance of the recording electrode array on the properties of the electrograms, and this needs to be considered in any further evaluation and analysis of the data; especially if considered for treatment such as electrogram-based ablations.

5.1. Study limitations

In this study, we modeled the 3D tissue of the atria as a 2D grid of cell assuming a constant electrode height of z_0 for the whole tissue that is under the electrode array. Although 3D forward tissue models of the atrial with varying values z_0 have already been developed in literature, employing them in an inverse problem for estimation of transmembrane current is not practical due to the complexity of these models. Moreover, that would require a proper estimation of z_0 for each recording site beforehand.

We did not have access to electrograms recorded from similar locations and different electrode sizes for a more complete evaluation of our results, as this is not possible in practice due to the temporal and spatial variations of the underlying wave propagation patterns during AF and especially for areas with complex fractionated electrograms.

The clinical electrograms used in this study were recorded from Bachmann's bundle with a predominant route of conduction from right to left and with a a potential role in AF [23] which may differ from the rest of atria. However, there are already regional differences in potentials in atria even during SR [24]. Although our method does not depend on these specific properties, the exact results in Tables 1–6 may not be generalizable to other regions in atria.

We used similar threshold values for evaluation of the measures introduced in Section 2.5 for simulated and real electrograms. Although both types of electrograms were scaled such that a homogeneous planar wave has a maximum absolute amplitude of 1 V, exact selection of these parameters is more prone to error in real electrograms as we do not have access to such exact recordings.

Moreover, we ignored the effect of noise in our simulations. Although smaller electrodes provide sharper and more localized recordings, they are affected more by noise and artifacts. Therefore, using a smaller electrode may not always improve the recordings.

Declaration of competing interest

None Declared.

References

[1] Y. Takahashi, M.D. O'Neill, M. Hocini, R. Dubois, S. Matsuo, S. Knecht, S. Mahapatra, K.-T. Lim, P. Jaïs, A. Jonsson, et al., Characterization of electrograms associated with termination of chronic atrial fibrillation by catheter ablation, J. Am. Coll. Cardiol. 51 (2008) 1003–1010.

[2] J.M. de Bakker, Electrogram recording and analyzing techniques to optimize selection of target sites for ablation of cardiac arrhythmias, Pacing Clin. Electrophysiol. 42 (2019) 1503–1516.

[3] E. Anter, C.M. Tschabrunn, M.E. Josephson, High-resolution mapping of scar-related atrial arrhythmias using smaller electrodes with closer interelectrode spacing, Circulation: Arrhythmia and Electrophysiology 8 (2015) 537–545.

[4] M. Hwang, J. Kim, B. Lim, J.-S. Song, B. Joung, E.B. Shim, H.-N. Pak, Multiple factors influence the morphology of the bipolar electrogram: an in silico modeling study, PLoS Comput. Biol. 15 (2019), e1006765.

[5] C.-Y. Lin, A.L.D. Te, Y.-J. Lin, S.-L. Chang, L.-W. Lo, Y.-F. Hu, F.-P. Chung, T.-C. Tuan, T.-F. Chao, J.-N. Liao, et al., High-resolution mapping of pulmonary vein potentials improved the successful pulmonary vein isolation using small electrodes and inter-electrode spacing catheter, Int. J. Cardiol. 272 (2018) 90–96.

[6] M. Huemer, D. Qaiyumi, P. Attanasio, A. Parwani, B. Pieske, F. Blaschke, L.-H. Boldt, W. Haverkamp, A. Wutzler, Does the extent of left atrial arrhythmogenic substrate depend on the electroanatomical mapping technique: impact of pulmonary vein mapping catheter vs. ablation catheter, Ep Europace 19 (2017) 1293–1301.

[7] M. Andronache, N. Drca, G. Viola, High-resolution mapping in patients with persistent af, Arrhythmia Electrophysiol. Rev. 8 (2019) 111.

[8] V. Jacquemet, C.S. Henriquez, Genesis of complex fractionated atrial electrograms in zones of slow conduction: a computer model of microfibrosis, Heart Rhythm 6 (2009) 803–810.

[9] D.D. Correa de Sa, N. Thompson, J. Stinnett-Donnelly, P. Znojkiewicz, N. Habel, J. G. Müller, J.H. Bates, J.S. Buzas, P.S. Spector, Electrogram fractionation: the relationship between spatiotemporal variation of tissue excitation and electrode spatial resolution, Circulation: Arrhythmia and Electrophysiology 4 (2011) 909–916.

[10] J.M. Stinnett-Donnelly, N. Thompson, N. Habel, V. Petrov-Kondratov, D.D.C. de Sa, J.H. Bates, P.S. Spector, Effects of electrode size and spacing on the resolution of intracardiac electrograms, Coron. Artery Dis. 23 (2012) 126–132.

[11] P.R. Rocha, P. Schlett, U. Kintzel, V. Mailänder, L.K. Vandamme, G. Zeck, H. L. Gomes, F. Biscarini, D.M. De Leeuw, Electrochemical noise and impedance of au electrode/electrolyte interfaces enabling extracellular detection of glioma cell populations, Sci. Rep. 6 (2016) 34843.

[12] J.J. Wiley, R.E. Ideker, W.M. Smith, A.E. Pollard, Measuring surface potential components necessary for transmembrane current computation using microfabricated arrays, Am. J. Physiol. Heart Circ. Physiol. 289 (2005) H2468–H2477.

[13] R. Plonsey, R.C. Barr, Bioelectricity: a Quantitative Approach, Springer Science & Business Media, 2007.

[14] N. Virag, V. Jacquemet, C. Henriquez, S. Zozor, O. Blanc, J.-M. Vesin, E. Pruvot, L. Kappenberger, Study of atrial arrhythmias in a computer model based on magnetic resonance images of human atria, Chaos: An Interdisciplinary Journal of Nonlinear Science 12 (2002) 754–763.

[15] M. Courtemanche, R.J. Ramirez, S. Nattel, Ionic mechanisms underlying human atrial action potential properties: insights from a mathematical model, Am. J. Physiol. Heart Circ. Physiol. 275 (1998) H301–H321.

[16] E. Vigmond, A. Pashaei, S. Amraoui, H. Cochet, M. Hassaguerre, Percolation as a mechanism to explain atrial fractionated electrograms and reentry in a fibrosis model based on imaging data, Heart Rhythm 13 (2016) 1536–1543.

[17] B. Abdi, R.C. Hendriks, A.-J. van der Veen, N.M. de Groot, A compact matrix model for atrial electrograms for tissue conductivity estimation, Comput. Biol. Med. 107 (2019) 284–291.

[18] E.A. Lanters, D.M. van Marion, C. Kik, H. Steen, A.J. Bogers, M.A. Allessie, B. J. Brundel, N.M. de Groot, Halt & reverse: hsf1 activators lower cardiomyocyt damage; towards a novel approach to reverse atrial fibrillation, J. Transl. Med. 13 (2015) 347.

[19] L.J. van der Does, A. Yaksh, C. Kik, P. Knops, E.A. Lanters, C.P. Teuwen, F.B. Oei, P. C. van de Woestijne, J.A. Bekkers, A.J. Bogers, et al., Quest for the arrhythmogenic substrate of atrial fibrillation in patients undergoing cardiac surgery (quasar study): rationale and design, Journal of cardiovascular translational research 9 (2016) 194–201.

[20] E.M. Mouws, E.A. Lanters, C.P. Teuwen, L.J. van der Does, C. Kik, P. Knops, J. A. Bekkers, A.J. Bogers, N.M. de Groot, Epicardial breakthrough waves during sinus rhythm: depiction of the arrhythmogenic substrate? Circulation: Arrhythmia and Electrophysiology 10 (2017), e005145.

[21] B. Abdi, R.C. Hendriks, A.-J. van der Veen, N.M. de Groot, Improved local activation time annotation of fractionated atrial electrograms for atrial mapping, Comput. Biol. Med. 117 (2020) 103590.

[22] B. Abdi, R.C. Hendriks, A.-J. van der Veen, N.M. de Groot, Local activation time annotation in atrial electrogram arrays using deconvolution, in: 2019 Computing in Cardiology (CinC), IEEE, 2019, pp. 1–4.

[23] C.P. Teuwen, A. Yaksh, E.A. Lanters, C. Kik, L.J. van der Does, P. Knops, Y. J. Taverne, P.C. van de Woestijne, F.B. Oei, J.A. Bekkers, et al., Relevance of conduction disorders in bachmann's bundle during sinus rhythm in humans, Circulation: Arrhythmia and Electrophysiology 9 (2016), e003972.

[24] M.S. van Schie, R. Starreveld, A.J. Bogers, N. de Groot, Sinus rhythm voltage fingerprinting in patients with mitral valve disease using a high-density epicardial mapping approach, EP Europace (2021) 469–478.